CrossMark

Atmospheric energetics over the tropical Indian Ocean during Indian Ocean dipole events

Yuehong Wang[1] · Jianping Li[1,2] · Yazhou Zhang[1] · Qiuyun Wang[1] · Jianhuang Qin[3]

Abstract
The evolution of atmospheric perturbation potential energy (PPE) over the tropical Indian Ocean is analyzed during a composite positive IOD event using reanalysis datasets for the period 1948–2015. The IOD modulates the variation in PPE, which then affects perturbation kinetic energy (PKE) through energy conversion. The PPE anomalies in the lower troposphere (1000–850 hPa) as the dominant layer of the PPE in the whole troposphere (1000–150 hPa) present a dipole pattern corresponding to the anomalous variation in SST during the IOD event. When cold SST anomalies (SSTAs) first appear in the eastern Indian Ocean (IOD-E), they reduce the atmospheric PPE in the lower troposphere rapidly. The negative PPE anomalies lead to less energy conversion to PKE, restraining the surface wind convergence over the IOD-E and weakening the climatological Walker circulation. Meanwhile, the surface easterly wind anomalies strengthen, which depresses the thermocline to the west and gives warmer SSTAs in the western Indian Ocean (IOD-W). The PPE anomalies and energy conversion (C_K) over the IOD-W are opposite to those over the IOD-E, the anomalous easterly wind continues to develop, and the positive SSTAs in the IOD-W reach a peak. Thus, the response of the Walker circulation over the Indian Ocean provides a positive feedback during the IOD event and explains the delayed effect of IOD-E SSTAs on IOD-W SSTAs.

1 Introduction

The Indian Ocean zonal dipole mode (IOD) is a dominant mode of the Indian Ocean on an interannual time scale (Saji and Goswami 1999; Webster et al. 1999; Drbohlav et al. 2007). The positive phase of the IOD is characterized by strong positive sea surface temperature anomalies (SSTAs) in the tropical western Indian Ocean and negative SSTAs in the tropical southeastern Indian Ocean, accompanied by pronounced anomalous easterlies over the central equatorial Indian Ocean. The positive IOD leads to drought over Indonesia and heavy rainfall and floods over East Africa, while the situation is reversed in the negative phase (Webster et al. 1999). The IOD has been studied extensively owing

to its great impact on the Asian monsoon (Li and Mu 2001; Guan and Yamagata 2002; Ashok et al. 2003, 2004; Saji and Yamagata 2003; Behera and Yamagata 2003; Yamagata et al. 2004; Ding et al. 2010; Li and Wu 2011a, b; Yang et al. 2015) and El Niño–Southern Oscillation (ENSO) (Ashok et al. 2001; Luo et al. 2010; Izumo et al. 2010; Dong et al. 2016; Wang et al. 2016; Zhou et al. 2017).

Previous researches on the interannual variability of IOD events focused on the changes in mixed layer depth or the temperature changes in the upper Indian Ocean (Li et al. 2002; Drbohlav et al. 2007; Rao et al. 2009; Hong et al. 2008a, b) and on its triggering mechanisms and processes of the related positive and negative feedback (Murtugudde et al. 2000; Annamalai et al. 2003; Saji and Yamagata 2003; Kumar et al. 1999; Zhang et al. 2018). The majority of these studies suggested that the Bjerknes feedbacks (Bjerknes 1966, 1969) may operate in the equatorial Indian Ocean (Webster et al. 1999; Li et al. 2003). This dynamic feedback involves interactions among the zonal SST gradient, the low-level zonal wind in the central equatorial Indian Ocean, and the east–west thermocline displacement. For example, negative SSTAs off Sumatra induce anomalous low-level easterlies in the central equatorial Indian Ocean, which depress (lift) the thermocline to the west (east).

✉ Jianping Li
ljp@bnu.edu.cn

[1] College of Global Change and Earth System Sciences (GCESS), Beijing Normal University, Beijing 100875, China

[2] Laboratory for Regional Oceanography and Numerical Modeling, Qingdao National Laboratory for Marine Science and Technology, Qingdao 266237, China

[3] Institute of Oceanography, Shanghai Jiao Tong University, Shanghai 200433, China

The raised thermocline to the east enhances SST cooling through upwelling of anomalously cold subsurface water. The enhanced surface cooling further amplifies the easterly wind anomalies. The IOD develops through this positive dynamic feedback. Given the great impact of the anomalous circulation on the evolution of an IOD event, it is important to explore the causes of the related abnormal atmospheric circulation to improve our understanding of the role of atmospheric processes in the dynamic feedback of the IOD. The long-term motion of the atmosphere is driven by the external energy supply, with friction acting to dissipate the motion (Peixóto and Oort 1974; Li and Chou 1997). It is therefore important to understand IOD dynamics from the perspective of energetics, as the generation and maintenance of the abnormal circulation are related to the transport and conversion of energy.

Earlier theories of atmospheric energetics have confirmed that external diabatic heating cannot be directly converted into kinetic energy of the atmosphere, suggesting that the underlying surface forcing is not a direct source of kinetic energy. In fact, only a small percentage of the total potential energy in the atmosphere can be converted into kinetic energy (Lorenz 1955; Oort 1964, 1971; Peixóto and Oort 1974), and the change in kinetic energy is directly related to changes in atmospheric circulation. Therefore, Lorenz (1955) proposed the concept of available potential energy (APE) to solve the problem of energy efficiency and formulated the modern framework of atmospheric energetics.

Several improvements have been made to extend Lorenz's classical theory to the local scale (Smith 1969a; Smith and Horn 1969b; Johnson 1970; Edmon 1978; Oort et al. 1989; Gu 1990; Hu et al. 2004). However, because these local APE theories still adopt the APE formulation, which defines the minimum total potential energy as the atmospheric reference state when the stratification is horizontal and statically stable (Lorenz 1955), this approach is not suitable for investigating local atmospheric energetics because the reference condition is ideal and physically unreachable (Gao et al. 2006). These limitations led Li and Gao (2006) to propose a more realistic concept of perturbation potential energy (PPE) by deducing some properties of atmospheric adiabatic processes under physical constraints. The PPE can better reflect the local energy efficiency than the APE theory (Gao and Li 2007, 2012, 2013; Li et al. 2016a, b; Dong et al. 2017; Wang et al. 2018). For instance, Wang et al. (2015) confirmed that PPE is an important link between non-adiabatic heating and local kinetic energy changes. And Dong et al. (2017) investigated the variability in tropical Pacific atmospheric energetics using PPE and suggested a possible negative feedback in the atmosphere during an ENSO cycle, which may explain the bursts of westerly or easterly wind that occur mainly in the western Pacific. Furthermore, Wang et al. (2012, 2015) used the baroclinicity of the atmosphere to introduce the concept of layer

perturbation potential energy (LPPE) by decomposing the PPE in the vertical direction. They further investigated the vertical structure of atmospheric PPE and applied the theory to explore the variability in the South China Sea summer monsoon and East Asian summer monsoon to explain the mechanisms controlling monsoon intensity (Huyan et al. 2017).

Given the importance of PPE theory for local dynamic processes and the fact that few studies have examined the atmospheric evolutionary processes of IOD events from the perspective of energy, the aim of this study is to investigate the spatial and temporal variations in atmospheric PPE and the effect of PPE on the local atmospheric circulation through energy conversion over the tropical Indian Ocean during an IOD event.

The remainder of this manuscript is organized as follows. Data and methodology are described in Sect. 2. The aim of Sect. 3 is to identify the relationship between SST and PPE during a composite IOD event, while Sect. 4 considers the important role of PPE as a link between the underlying external forcing and local kinetic energy. Section 5 describes the temporal and spatial evolution of PPE and the interrelation of PPE in different layers. The possible mechanism by which PPE affects atmospheric circulation anomalies is discussed in Sect. 6, followed by the main conclusions and discussion in Sect. 7.

2 Data and methodology

2.1 Data

This study employs monthly average datasets including temperature, winds, vertical velocity, and surface pressure from the National Centers for Environmental Prediction–National Center for Atmospheric Research (NCEP/NCAR) reanalysis (Kalnay et al. 1996). The horizontal grid resolution is $2.5° \times 2.5°$ and there are 11 levels (1000–150 hPa) in the vertical. The SST data is from the Hadley Centre sea ice and sea surface temperature (HadISST) datasets (Rayner et al. 2003) with a grid resolution of $1° \times 1°$. The period covered is from January 1948 to December 2015.

2.2 Methodology

By considering some important properties of an adiabatic atmosphere, Li and Gao (2006) proposed the PPE as the difference in atmospheric total potential energy (TPE) between the actual state and the conditional minimum reference state via adiabatic redistribution, which is related to the state of the atmosphere before redistribution. We thus obtain a mathematical expression for PPE in isobaric coordinates as follows:

$$PPE_i = \frac{p_{00}^{(i-1)k} \prod_{j=0}^{i-1}(1+\kappa-j)}{i!\gamma_d(1+\kappa)} \int_0^{p_s} \frac{T'^i}{p^{(i-1)(1+\kappa)}} \left(-\frac{\partial\overline{\theta}}{\partial p}\right)^{-i+1} dp,$$

(1)

where $PPE_i (i = 1, 2, \ldots)$ is the ith moment term of PPE. Here, p is pressure; T is temperature; p_{00} is the reference pressure (usually taken as 1000 hPa); $\kappa = R/C_p$, where R is the gas constant of dry air and C_p is the specific heat at constant pressure; $\gamma_d = g/C_p$ is the dry adiabatic lapse rate; and $\theta = T(p_{00}/p)^\kappa$, where θ is potential temperature. T' is the perturbation temperature from the reference state and p_s is the surface pressure. The first- and second-moment terms of PPE are expressed as

$$PPE_1 = \frac{1}{\gamma_d} \int_0^{p_s} T' dp, \tag{2}$$

$$PPE_2 = \frac{\kappa p_{00}^\kappa}{2\gamma_d} \int_0^{p_s} \frac{T'^2}{p^{(1+\kappa)}} \left(-\frac{\partial \bar{\theta}}{\partial p} \right)^{-1} dp. \tag{3}$$

Note that the global average of PPE_1 is zero and the values of the global average of PPE_2 are equal to the value of the APE, while on the regional scale, PPE_1 is the dominant term of PPE and is an order of magnitude larger than the second-order term and other higher-moment terms that can be neglected (Li and Gao 2006). Therefore, PPE may be approximated by the sum of PPE_1 and PPE_2.

The governing equations of PPE and atmospheric perturbation kinetic energy (PKE) are as follows:

$$PPE = C_K + G + HBF_{PPE}, \tag{4}$$

$$PKE = -C_K + D + HBF_{KE}, \tag{5}$$

where $PKE = KE - \overline{KE}$, and $KE = \frac{1}{2g} \int_0^{p_s} \vec{V}^2 dp$, C_K represents the energy conversion between PPE_1 and PKE:

$$C_K = \frac{1}{g} \int_0^{p_s} (\omega\alpha - \overline{\omega\alpha}) dp, \tag{6}$$

where ω is the vertical velocity in pressure coordinates and α is the air specific volume. When C_K is positive, cold air ascends or warm air descends and energy is converted from PKE to PPE; conversely, when C_K is negative, warm air ascends or cold air descends and PPE is converted to PKE. Here also, G is the diabatic heating to the atmosphere and D represents viscous dissipation. The *HBF* terms stand for the horizontal boundary flux. The governing equations show that the change of external non-adiabatic heat (ΔG) will lead to the change of PPE (ΔPPE) directly, then changing the term of C_K (ΔC_K). As the bridge of the energy conversion between PPE and PKE, ΔC_K will lead to ΔPKE, and ΔPKE mainly manifests in the change of initial atmospheric circulation.

In view of the baroclinic of the atmosphere, the local energy distribution is also significantly abnormal in the vertical direction. Therefore, the atmospheric PPE is studied in different layers (Wang et al. 2012). The precise definition of layer PPE is as follows:

$$LPPE_1 = \frac{1}{\gamma_d} \int_{p_1}^{p_2} T' dp \tag{7}$$

$$LPPE_2 = \frac{\kappa p_{00}^\kappa}{2\gamma_d} \int_{p_1}^{p_2} \frac{T'^2}{p^{(1+\kappa)}} \left(-\frac{\partial \theta}{\partial p} \right)^{-1} dp \tag{8}$$

p_1 and p_2 are the lower and upper limits of the vertical integration over the pressure range, respectively. $LPPE = LPPE_1 + LPPE_2$. Similarity layer C_K and PKE can be obtained through changing the range of vertical integration.

In the present study, the monthly mean climatology is first calculated for the period 1948–2015 and anomalies are then defined as departures from this climatology. A procedure is applied to the data to remove a linear warming trend in the Indian Ocean (Saji and Yamagata 2003). A 5-month running mean and a 7-year high pass filter are then applied to all datasets to remove the intraseasonal and interdecadal variation, respectively. Following Saji and Goswami (1999), the dipole mode index (DMI) is defined as the difference in SSTAs between the tropical western Indian Ocean (10°S–10°N, 50°–70°E, hereafter referred to as the west pole of the IOD, IOD-W) and the eastern Indian Ocean (10°S–0°, 90°–110°E, hereafter referred to as the east pole of the IOD, IOD-E). Based on this index, the years 1961, 1963, 1972, 1976, 1982, 1983, 1987, 1991, 1994, 1997, and 2006 are selected to represent the major positive IOD events, and 1958, 1960, 1964, 1971, 1992, 1996, and 1998 to represent the major negative IOD events (Saji and Yamagata 2003). These positive and negative IOD years are referred to as IOD-years, and other (non-IOD) years as nIOD-years. To further investigate the relations among SST, PPE and PKE, a PPE anomalies dipole-like index (PDI) is defined as the difference in the normalized area-averaged PPE anomalies between the western Indian Ocean (15°S–15°N, 60°–80°E) and southeastern Indian Ocean (15°S–0°, 100°–120°E):

$$\begin{aligned} PDI = {} & PPE \text{ anomalies}_{(15°S-15°N, 60°-80°E)} \\ & - PPE \text{ anomalies}_{(15°S-0°, 100°-120°E)}, \end{aligned}$$

and the PKE anomalies index (PKEI) is defined as the normalized area-averaged PKE anomalies over the equatorial Indian Ocean (10°S–10°N, 70°–90°E). We define PDI (lower) for the lower (1000–850 hPa) troposphere and PDI (middle–upper) for the middle–upper (600–200 hPa) troposphere.

## 3 Delayed effect of IOD-E SSTAs on IOD-W SSTAs

For the convenience of the following discussion and to introduce the delayed effect of IOD-E SSTAs on IOD-W SSTAs, the evolution of composite SSTAs and surface wind anomalies associated with the IOD are displayed in Fig. 1. Although these features are well-known, we use this figure to set the scene here for the complex problem addressed in this study. Some of the main features are as follows. Cold SSTAs first appear surrounding the Indonesian islands by May–June, especially in the Java upwelling area (i.e. the IOD-E), accompanied by southeasterly wind anomalies in the southeastern Indian Ocean (Fig. 1a). The cold SSTAs continue to develop and move to the equator along the Indonesian coastline from July to August. Meanwhile, SSTAs become larger in the IOD-W accompanied by strengthened equatorial easterly wind anomalies (Fig. 1b); the IOD peaks in September–October (Fig. 1c) and then rapidly vanishes (Fig. 1d). These are essentially the same features as seen in previous studies (Saji and Goswami 1999; Hong et al. 2008a, b). The SSTAs in the IOD-E and IOD-W vary oppositely and the IOD-E SSTAs lead the IOD-W SSTAs during the composite IOD event. However, there is no significant negative correlation between the IOD-E SSTAs and IOD-W SSTAs. In addition, the lead–lag correlation between the

IOD-E SSTAs and IOD-W SSTAs indicates significant simultaneous positive correlations, and the maximum positive correlation occurs when the IOD-E lags IOD-W by 3–4 months (Fig. 2), indicating that the western and eastern parts of the Indian Ocean are more likely to have SSTAs of the same sign. This is consistent with previous results (Nicholls and Drosdowsky 2001; Dommenget and Latif 2002; Feng and Meyers 2003; Krishnamurthy and Kirtman 2003). Why then are the results of the composite and correlation analyses inconsistent?

To examine this question, the lead–lag correlations between IOD-E SSTAs and IOD-W SSTAs for IOD-years and nIOD-years are displayed in Fig. 2. The maximum negative correlation ($r = -0.34$) in IOD-years occurs when IOD-E SSTAs lead IOD-W SSTAs by 2 months, which is totally different from the results for all years and for nIOD-years. This implies that during the IOD events there is a delayed effect of IOD-E SSTAs on IOD-W SSTAs; i.e., cold SSTAs in the IOD-E first develop, then warm SSTAs in the IOD-W gradually grow, reaching their peak after 2 months, which is consistent with the composite analysis above. However, in nIOD-years there is significant simultaneous positive correlation between the IOD-E and IOD-W, and the maximum positive correlation occurs when IOD-E SSTAs lag IOD-W SSTAs by 2 months. These results indicate that the evolution of SSTAs in the IOD-E and IOD-W during IOD years is entirely different from
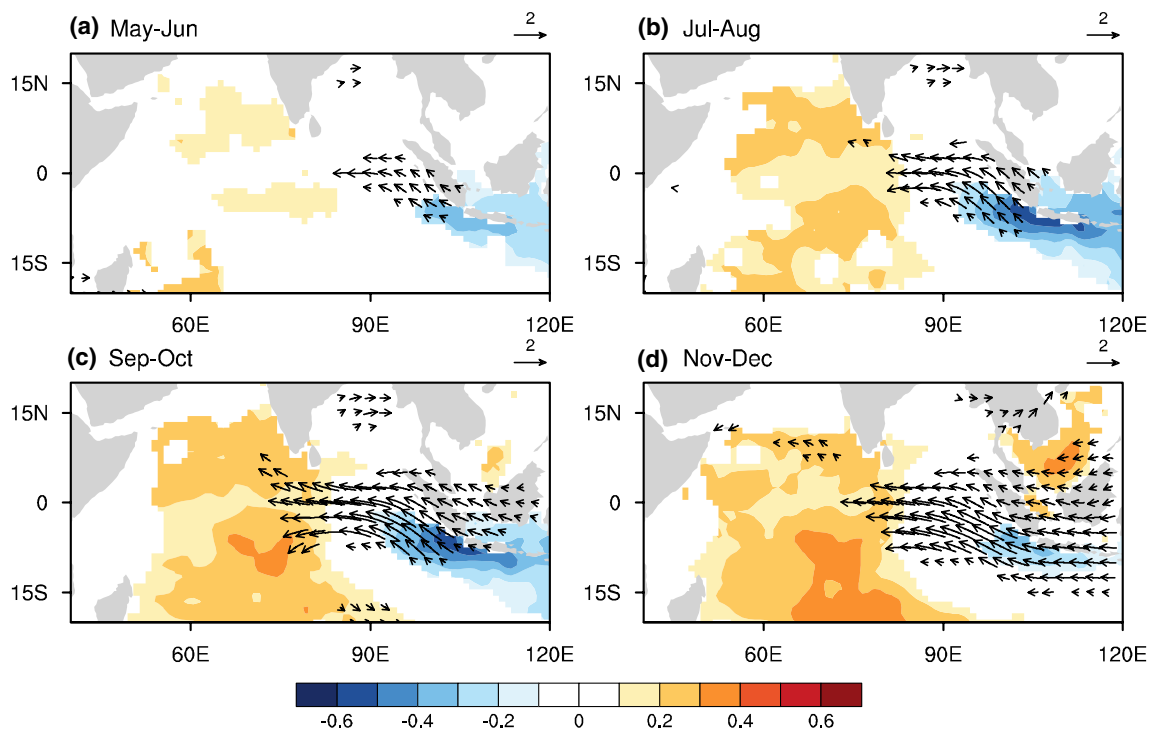
Fig. 1 Evolution of composite SSTAs (°C) and low-level (1000–850 hPa) wind anomalies (m s⁻¹) in **a** May–Jun, **b** Jul–Aug, **c** Sep–Oct, and **d** Nov–Dec during positive IOD events. The shaded areas and arrows are significant at the 99% level (Student's t-test)
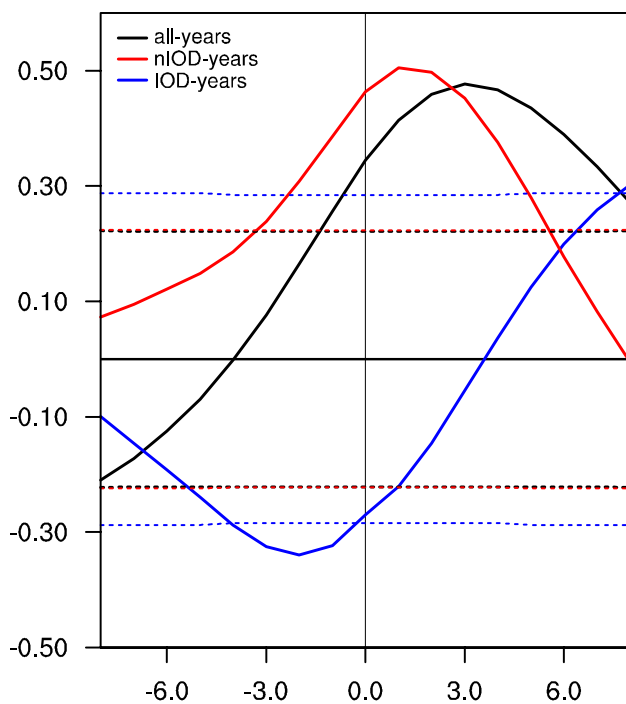
Fig. 2 Lead–lag correlations between the SSTAs in the IOD-E and IOD-W (negative lags denote IOD-E leading IOD-W). Solid black, blue, and red lines are for all-years, IOD-years, and nIOD-years, respectively. The dashed lines represent the 95% confidence levels based on the effective numbers of degrees of freedom

that during nIOD-years. This explains the lack of negative correlation between IOD-E SSTAs and IOD-W SSTAs in previous studies, as it is due to the influence of nIOD-years, which make up more than 70% of the time series so that there is a positive correlation between IOD-E SSTAs and IOD-W SSTAs when all years are included. In the following we will further elaborate on this delayed effect of IOD-E SSTAs on IOD-W SSTAs from the perspective of energetics.

4 Linking role of PPE during an IOD event

Figure 3 shows correlations of the DMI with atmospheric PPE anomalies in different layers and PKE anomalies over the whole troposphere over the equatorial Indian Ocean. The most prominent features are the significant negative correlation between PPE anomalies in the lower troposphere (1000–850 hPa) and DMI over the southeastern Indian Ocean (15°S–0°, 100°–120°E), and positive correlation over the western Indian Ocean (15°S–15°N, 60°–80°E). In the middle–upper troposphere (600–200 hPa), Fig. 3b shows that the region of positive correlation is located mainly over the western Indian Ocean and there is insignificant correlation over the southern Indian Ocean. In contrast, we note that the region of correlation between PPE anomalies of the
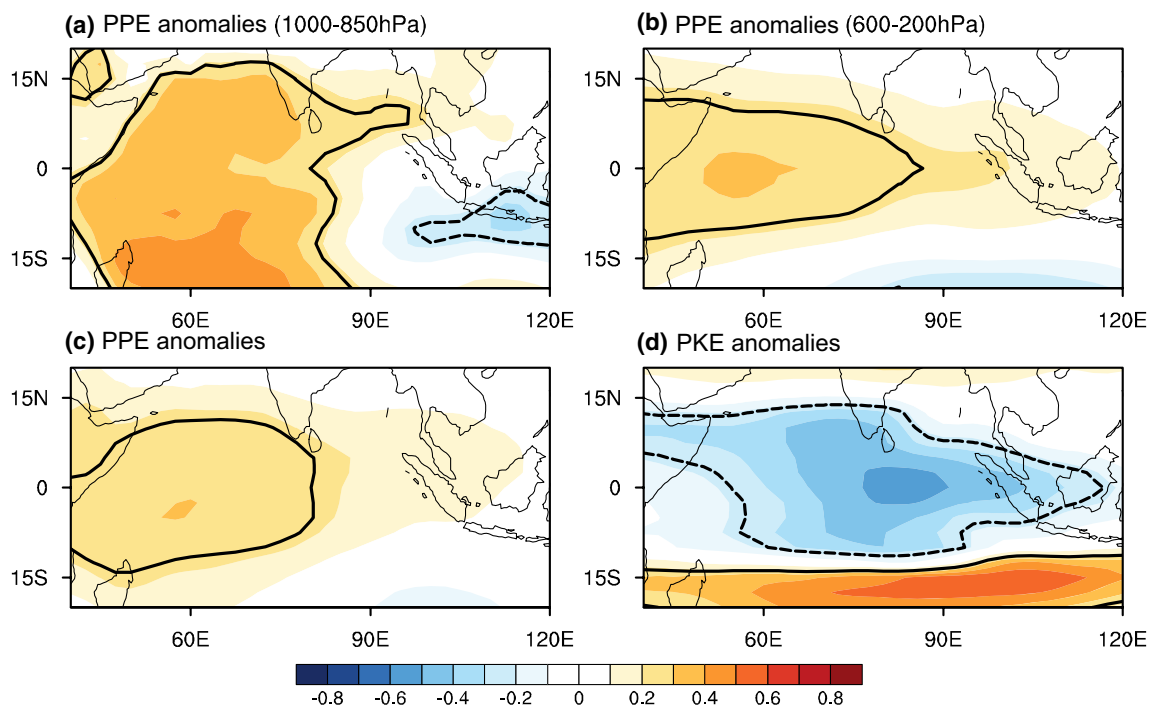
Fig. 3 Correlations between the DMI and **a** PPE anomalies in the lower troposphere (1000–850 hPa), **b** PPE anomalies in the middle–upper troposphere (600–200 hPa), **c** PPE anomalies in the whole troposphere (1000–150 hPa), and **d** PKE anomalies. The areas enclosed by solid lines are statistically significant at the 99% confidence level (Student's *t*-test)

whole troposphere (1000–150 hPa) and DMI is similar to that of the upper troposphere; i.e., mainly over the western Indian Ocean (Fig. 3c). These results suggest that when a positive IOD event occurs, the SSTAs are cold in the southeastern Indian Ocean and warm in the western Indian Ocean, and there is also a corresponding dipole pattern of PPE anomalies in the lower troposphere (1000–850 hPa). However, the PPE anomalies in the middle–upper troposphere (600–200 hPa) do not change over the eastern Indian Ocean and the PPE anomalies over the western Indian Ocean are positive. The PPE anomalies of the whole troposphere (1000–150 hPa) seem to have similar features to the PPE anomalies in the middle–upper troposphere (600–200 hPa). These are only simultaneous correlations and the relationship of PPE anomalies between the whole troposphere (1000–150 hPa) and different layers are discussed in detail below.

Correlations between the DMI and PKE anomalies over the whole troposphere are shown in Fig. 3d. Negative correlations dominate the equatorial Indian Ocean, which means that PKE anomalies decrease when an IOD occurs. Although there is a significant positive correlation away from the equator, this will not be discussed further, as we focus on the energy changes of the equatorial Indian Ocean.

Figure 4a illustrates the lead–lag correlation coefficients between the DMI, PDIand PKEI over the whole troposphere. It is clear that the KEI has the largest negative coefficients with DMI and PDI for simultaneous correlations, indicating that SST and PPE have important effects on PKE during the IOD event. To further study the relationships between PDI, DMI, and PKEI over the whole troposphere, partial correlations are also calculated. As shown in Fig. 4b, the connection between DMI and PDI is slightly affected by removing the effect of PKEI, which suggests that the IOD has a significant control on PPE. In contrast, the partial correlations between

DMI and PKEI change drastically when the effect of the PDI (over the whole troposphere) is removed. This indicates that PPE plays a major role in the influence of IOD on PKE. In addition, the partial correlations between PDI and PKEI become insignificant after removal of the SSTA signal. These results suggest that the physical linkage between PPE and PKE is more direct than that between the IOD and PKE. The variation in PPE is modulated by the IOD, and the PPE can then affect PKE through energy adjustment and conversion.

5 Evolution of PPE during the IOD event

5.1 Temporal variation in PPE

To further investigate the relationship between SST and PPE, and the relationship of PPE in different layers of the troposphere during the IOD event. Figure 5a shows the standardized time series of PDI (lower) and DMI, and Fig. 5d their lead–lag correlations. Generally, in the most years, there are extremes of positive PDI (lower) when a strong positive IOD event occurs, and the conditions are reversed in the negative phase (Fig. 5a). Notably, DMI has the largest positive correlation with PDI (lower) at zero lag ($r = 0.60$) (Fig. 5d). In contrast, the amplitude of PDI (middle–upper) changes relatively smaller (Fig. 5b) and the largest positive correlation with DMI is 0.38 when the PDI (middle–upper) lags DMI by $1-2$ month (Fig. 5e). Over the whole troposphere, PDI is more consistent with DMI changes (Fig. 5c), and the largest positive correlation with DMI is 0.66 at zero lag (Fig. 5f). The correlation reduces significantly after the PDI (lower) signal is removed, as shown by the dashed line in Fig. 5f, and PDI (lower) explains more than 60% of the total variance of PDI, while the correlation reduces a little after removing the PDI (middle–upper) signal. These results suggest that the PPE anomalies of the whole troposphere have a

Fig. 4 **a** Lead–lag correlations between the DMI and PDI (long dashes), DMI and PKEI (solid line), and PDI and PKEI (short dashes). **b** Same as **a**, but for partial correlations. $r(X, Y)$ is the correlation between the variables X and Y, and $pr(X, Y/Z)$ is the partial correlation between X and Y with the variable Z removed. The horizontal dashed lines are 99% confidence levels (Student's t-test)
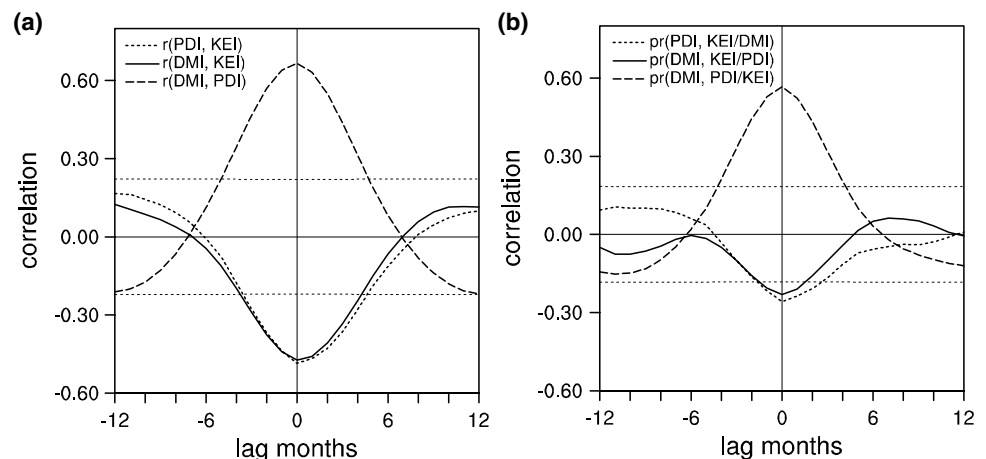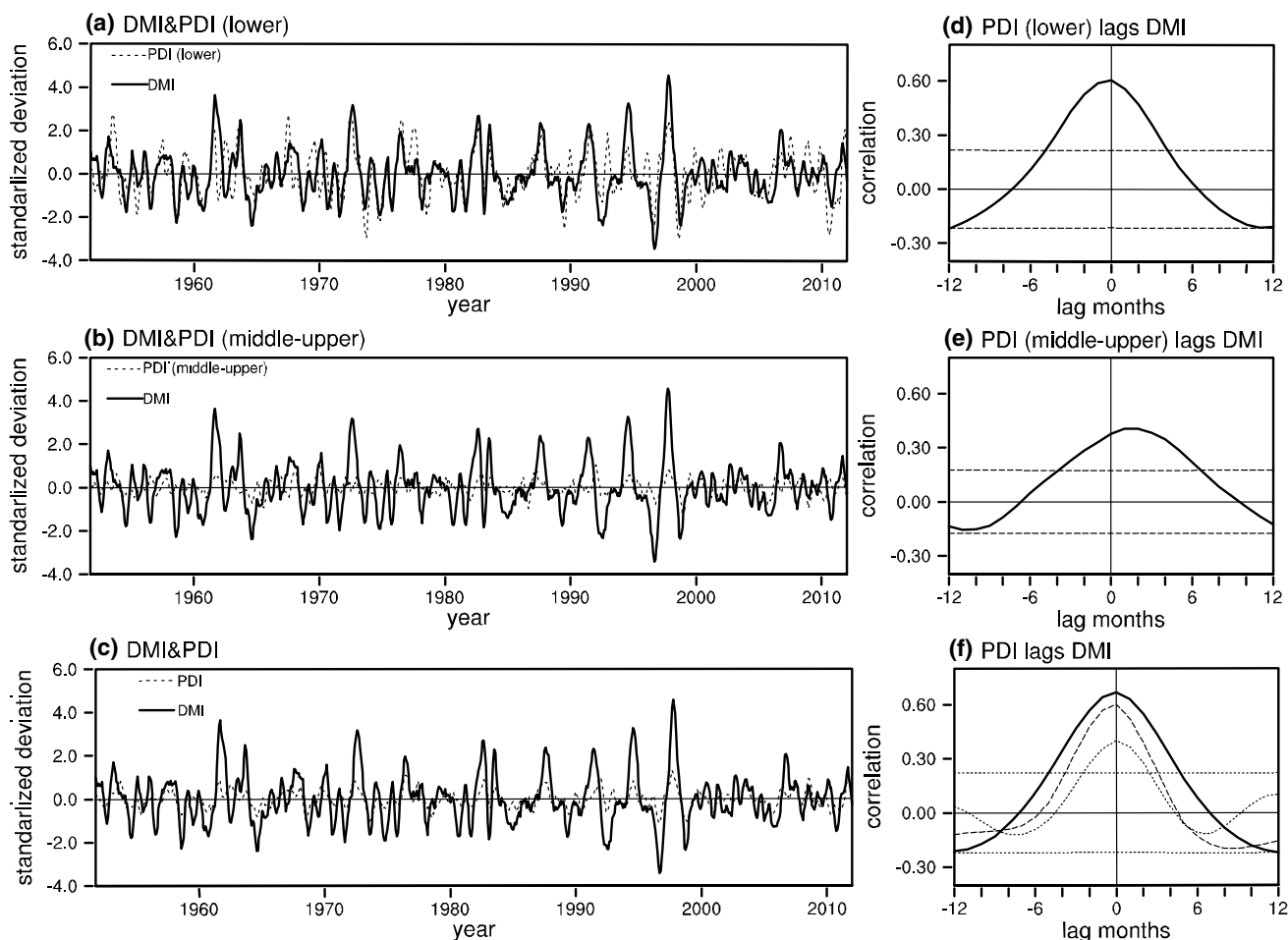
Fig. 5 Standardized time series of the DMI and **a** PDI (lower, 1000–850 hPa), **b** PDI (middle–upper, 600–200 hPa), and **c** PDI (1000–150 hPa) during the period 1948–2015. Lead–lag correlation (thick solid lines) between the DMI and **d** PDI (lower), **e** PDI (middle–upper), and **f** PDI (1000–150 hPa). In **f** the thin dashed line is the partial correlation with the PDI (middle–upper) removed, and the dotted line is the partial correlation with the PDI (lower) removed. The horizontal dashed lines in **d**–**f** are 99% confidence levels (Student's *t*-test)

coherent response to the SSTAs during the IOD event, and there is no lag on the monthly scale. The high value of variance and the simultaneity indicate that the PPE anomalies in the lower troposphere are the dominant layers affecting the distribution of PPE anomalies of the whole troposphere.

5.2 Spatial variation in PPE

To compare the evolution of SSTAs and PPE anomalies during the IOD event, Fig. 6 shows the composite SSTAs and PPE anomalies (1000–850 hPa) for the 11 extremely positive IOD events mentioned in Sect. 2. At the initial stage of the positive IOD event (Fig. 6a), negative PPE anomalies and SSTAs in the southeastern Indian Ocean occur at the same time as positive PPE anomalies in the southwestern Indian Ocean. As the SSTAs intensify in the Indian Ocean, PPE anomalies develop into an evident dipole pattern over the tropical Indian Ocean, consistent with the distribution of

SSTAs from July to August (Fig. 6b). Then, from September to October (Fig. 6c), the SSTAs in the eastern Indian Ocean reach their peak while those in the western Indian Ocean continue to increase, as negative PPE anomalies weaken over the eastern Indian Ocean and positive PPE anomalies expand eastwards over the western Indian Ocean. After October (Fig. 6d), the SSTAs in the Indian Ocean weaken rapidly and warmer SSTAs in the western Indian Ocean expand eastwards, showing a tendency to Indian Ocean basin mode, and positive PPE anomalies continue to expand eastwards over the western Indian Ocean, ultimately covering the entire Indian Ocean. During the evolution of the IOD, the temporal and spatial characteristics of the PPE anomalies (1000–850 hPa) are essentially the same as those of the SSTAs.

Figure 7 shows the composite middle–upper PPE anomalies (600–200 hPa). Positive PPE anomalies change significantly until July and mainly dominate the region over
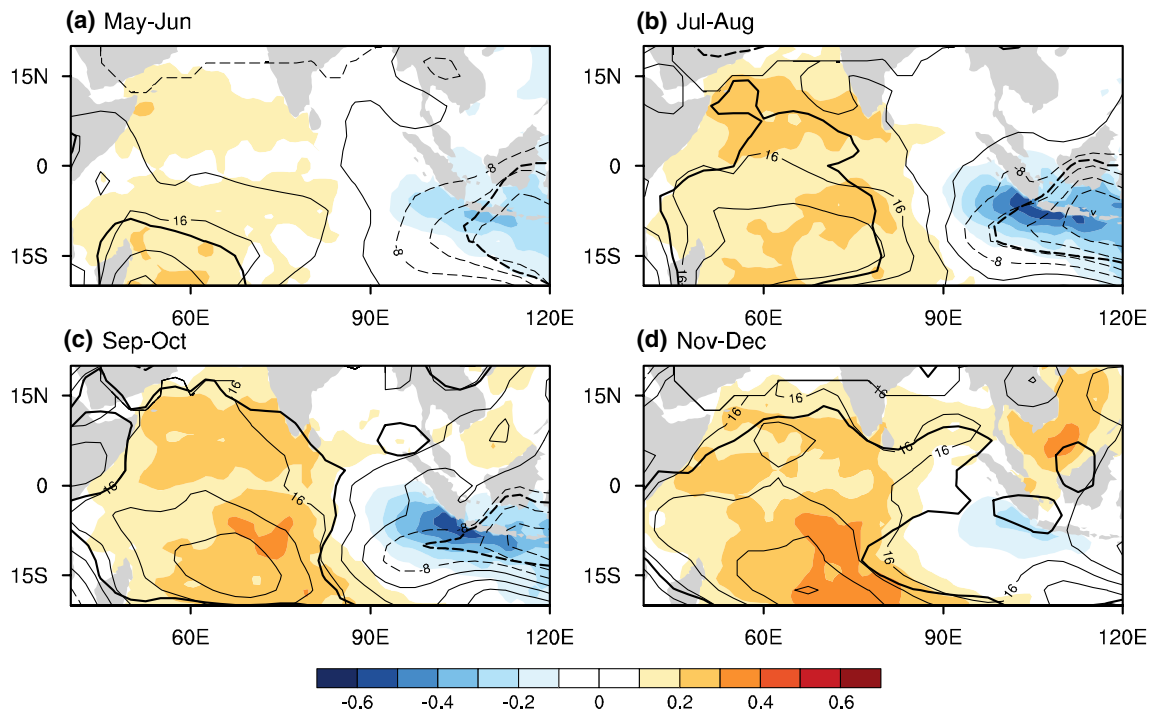
Fig. 6 Evolution of composite SSTAs (shading, °C) and lower tropospheric (1000–850 hPa) PPE anomalies (contours, 10^4 J m^{-2}) in **a** May–Jun, **b** Jul–Aug, **c** Sep–Oct, and **d** Nov–Dec during the positive IOD event. The shaded areas and arrows are significant at the 99% level (Student's *t*-test)
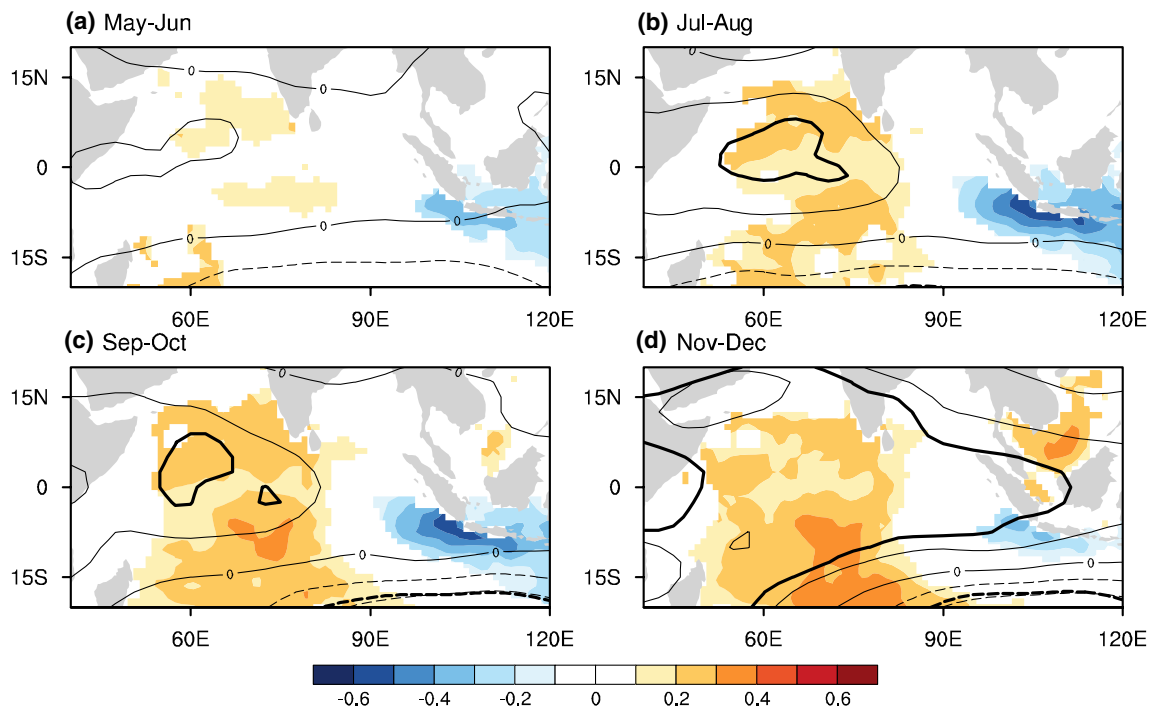

Fig. 7 Same as Fig. 6, but for the middle–upper (600–200 hPa) tropospheric PPE anomalies

the western Indian Ocean (Fig. 7b). The change of PPE in the middle–upper troposphere lags that at 1000–850 hPa. The evolution of composite PPE anomalies of the whole troposphere (1000–150 hPa) during the IOD event is similar to that of the PPE anomalies in the lower troposphere (not shown). The above results show that when the IOD event occurs, the strongest response of the PPE anomalies of the whole troposphere (1000–150 hPa) is in the lower layer of the troposphere where the changes are consistent with those of the SSTAs. To better explore the vertical evolution of the PPE anomalies over the western and eastern Indian Ocean during the IOD event, Fig. 8 shows time–height plots of composite PPE anomalies over the IOD-W and IOD-E during the positive IOD event. In the lower troposphere (1000–850 hPa), positive PPE anomalies in the IOD-W appear after June, then peak in September and persist until the next year. Significantly negative PPE anomalies in the IOD-E start much earlier than May, peak in July and August, weaken rapidly during September to October, and sharply translate into positive PPE anomalies in December (Fig. 8b). Moreover, in the middle–upper troposphere (600–200 hPa), positive PPE anomalies in the IOD-W occur 2–3 months later than the lower tropospheric PPE anomalies, and then gradually intensify until the next year, whereas no such features are found in the IOD-E. These results indicate that the negative PPE anomalies in the IOD-E are located mainly in the lower troposphere, corresponding to the cooling SSTAs in the IOD-E, while positive PPE anomalies in the IOD-W are significant over the whole troposphere, corresponding to the warmer SSTAs in the IOD-W. However, the changes of PPE anomalies in the middle–upper troposphere lag those in the lower troposphere.

6 Energetic effects on atmospheric circulation

The atmospheric PPE, as a key link between the local underlying external forcing and the variability in PKE, is expected to influence the atmospheric circulation over the tropical Indian Ocean. Figure 9a shows the lead–lag correlations between DMI and low-level zonal wind anomalies (U-wind), and their partial correlation with the effect of PDI removed. Note that the correlation of DMI and U-wind is highly significant ($r = -0.68$) when U-wind lags by 1 month. After the PDI signal is removed (black dashed line), the relationship between them clearly weakens. Furthermore, the lead–lag correlations between U-wind and SSTAs in the IOD-E and IOD-W show that the U-wind occurs simultaneously with the IOD-E SST and leads the IOD-W SST by 2 months, which suggests that the U-wind develops consistently with the IOD-E SST and enhances positive SSTAs in the IOD-W 2 months later. The weakened partial correlations indicate that the PPE serves as a bridge linking the Indian Ocean SSTAs and the zonal wind anomalies over the equatorial Indian Ocean. The correlations between U-wind and SSTAs in the IOD-E and IOD-W suggest that the zonal wind anomalies may further influence the evolution of the IOD through air–sea interaction. The same characteristics can be demonstrated in the temporal evolution (Fig. 9b). The intensity of the U-wind is remarkably high along with highly negative SSTAs in the IOD-E during May–July, and then the SSTAs in the IOD-W continue warming, rapidly enhancing the U-wind that peaks in October, and then drops. After removing the PDI signal, the intensity of U-wind decreases significantly, the weakened circulation decreases the depression of the thermocline to the west, at the same time, wind stress curl also make some contribution to the change of the thermocline (not shown). Thereby the SSTAs in the IOD-W
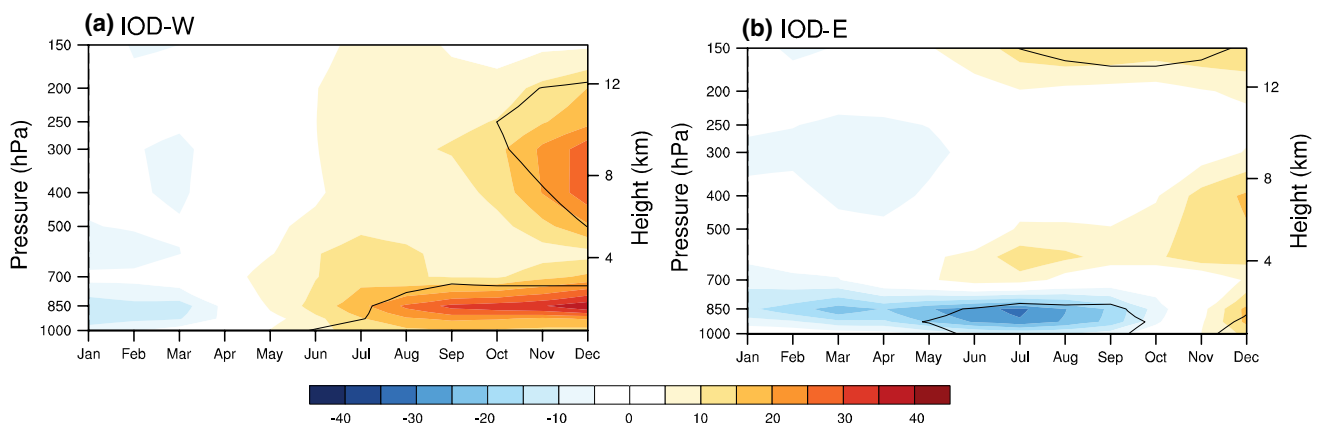
Fig. 8 Time–height plots of composite PPE anomalies (10^4 J m^{-2}) over **a** the IOD-W and **b** IOD-E during the positive IOD event. The areas surrounded by the solid lines are statistically significant at the 99% level (Student's t-test)
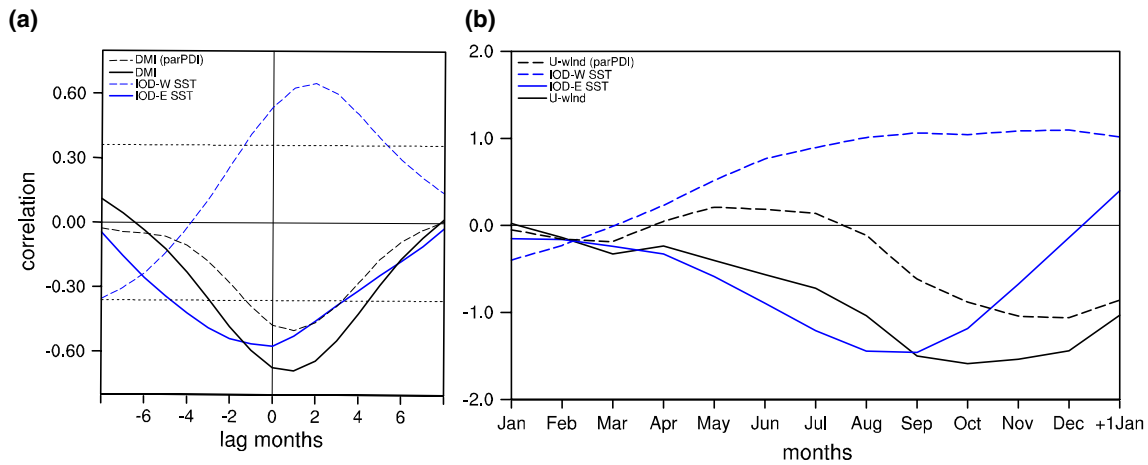
Fig. 9 **a** Lead–lag correlations of U-wind (5°S–5°N, 70°–90°E, 1000–850 hPa) with the DMI (black solid line), the DMI after the PDI is removed (black dashed line), IOD-W SST (blue dashed line), and IOD-E SST (blue solid line) for IOD-years. The thin horizontal dashed lines are 99% confidence levels (Student's *t*-test). **b** Time evolution of composite standardized IOD-E SST (blue solid line), IOD-W SST (blue dashed line), U-wind (black solid line) and U-wind with the PDI removed (black dashed line) during the positive IOD event

decrease. The anomalous easterlies are not strengthened in October, and thus the IOD cannot develop.

Equation (5) demonstrates that energy can be converted between PPE and PKE through C_K, which is approximately equal to the PKE variation that drives atmospheric circulation. Figure 10 presents the evolution of the composite

anomalous atmospheric circulation and C_K during the IOD event in the form of longitude–pressure cross-sections along 5°S–5°N. In Fig. 10a, b, positive C_K is located over the eastern Indian Ocean with significant downward motion, and zonal winds begin to strengthen during July and August. As the IOD event enters its mature phase (Fig. 10c), the
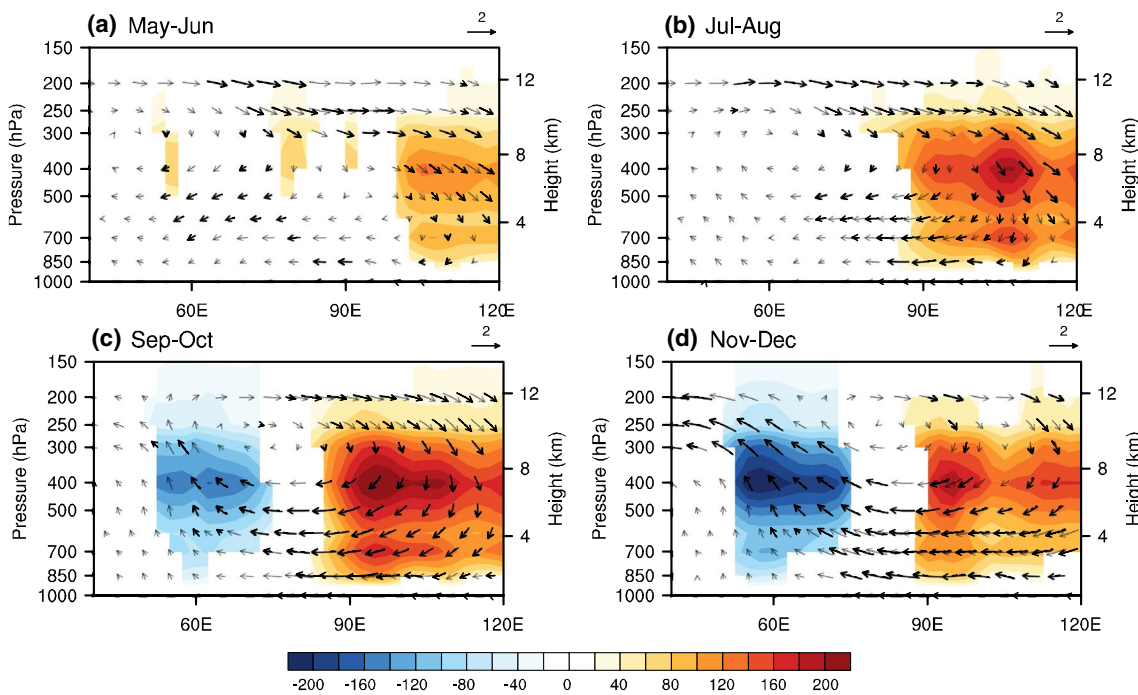
Fig. 10 Evolution of composite C_K (W m^{-2}) and zonal circulation (arrows) averaged over 5°S–5°N in **a** May–Jun, **b** Jul–Aug, **c** Sep–Oct, and **d** No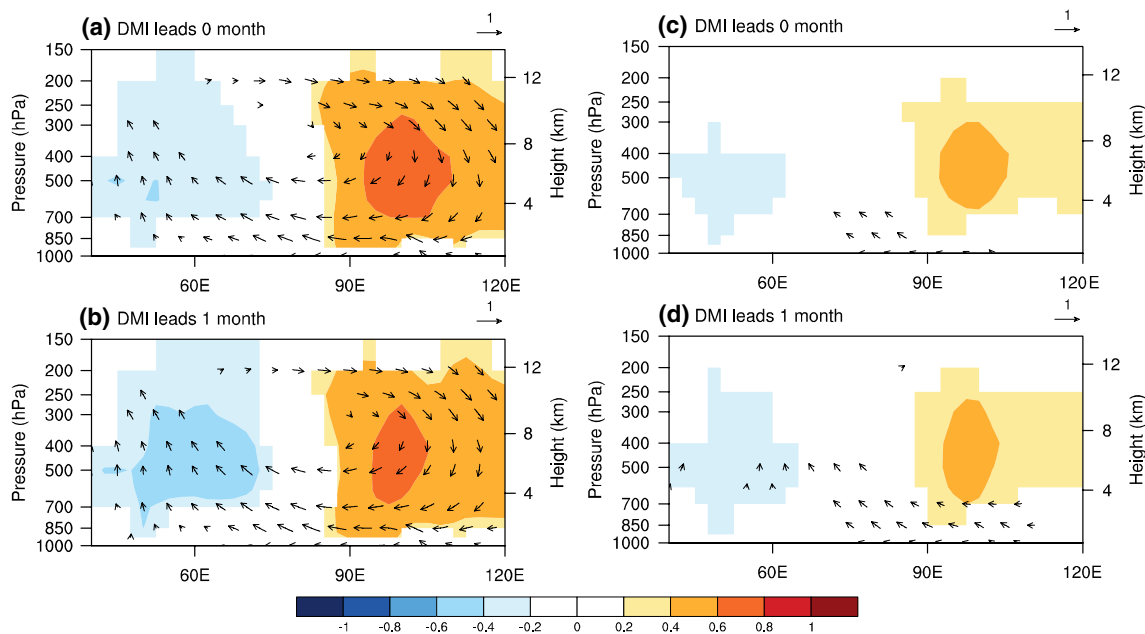v–Dec during the positive IOD event. Anomalies in C_K and zonal circulation exceeding the 99% confidence level (Student's *t*-test) are indicated by shading and bold arrows, respectively

region and value of positive C_K over the IOD-E reach their maximum. In contrast, C_K is negative over the IOD-W and the anomalous circulation over the Indian Ocean is characterized by easterly anomalies in the lower troposphere and westerly anomalies aloft, with downward anomalies over the Maritime Continent and upward anomalies over the IOD-W; this opposes the climatological Walker circulation over the tropical Indian Ocean. During November and December (Fig. 10d), negative C_K over the IOD-W reaches its maximum magnitude, while the anomalous circulation continues to develop and easterly wind anomalies in the lower troposphere are evident over the whole equatorial Indian Ocean. The opposite energy conversion processes over the IOD-E and IOD-W indicate that the changes in atmospheric PPE have different influences on the atmospheric circulation, especially the surface wind stresses that are of great importance in IOD dynamics. Over the IOD-E, when C_K is positive, the atmospheric PKE decreases, weakening the lower level convergence of the climatological Walker circulation over the IOD-E, and anomalous surface easterly wind develops. The change in C_K over the IOD-W occurs later than over the IOD-E. When C_K is negative over the IOD-W, atmospheric PKE increases, further enhancing the lower-level anomalous convergence (similar results can be obtained when the ERA-Interim datasets are employed, not shown here). The climatological Walker circulation

continues to weaken and the anomalous easterly wind reaches its maximum.

To further quantify the statistical relation of the PPE anomalies with C_K and atmospheric circulation, the lead–lag correlations between DMI and the 40°–120°E equatorial zonal circulation and C_K, and the correlations with the PDI signal removed, are presented in Fig. 11. The maximum positive DMI is concurrent with the maximum positive C_K in the IOD-E (Fig. 11a), indicating that fewer PPE anomalies can convert into PKE when the SSTAs are negative, while negative C_K occurs in the IOD-W, leading to more energy converting into PKE, thereby generating an anomalous Walker circulation. A month later (Fig. 11b), the negative C_K in the IOD-W peaks, which leads to enhancement of the anomalous Walker circulation, resulting in a rapid strengthening of anomalous easterly wind. After the PDI is removed, as shown in the right panels of Fig. 11, the C_K intensity decreases sharply and the anomalous Walker circulation almost vanishes. These results suggest that the energy conversion processes over the IOD-E and IOD-W provide a positive feedback to the development and maintenance processes of IOD evolution.

The schematic diagram in Fig. 12 illustrates the positive feedback during a positive IOD event. When a typical positive IOD event develops in the tropical Indian Ocean, cool SSTAs first appear in the IOD-E, rapidly deceasing the atmospheric PPE in the lower troposphere, and negative PPE anomalies lead to less energy converting into PKE, weakening the surface wind convergence over the IOD-E

Fig. 11 **a** Correlations of the DMI with C_K (shading) and zonal circulation (arrows). **b** Same as **a**, but for the DMI leading by 1 month. **c** Same as **a**, but with the PDI signal removed. **d** Same as **b**, but with the PDI signal removed. Values exceeding the 99% confidence level (Student's t-test) are indicated by shading and arrows

Fig. 12 Schematic diagram of atmospheric energy variation and corresponding circulation and SST anomalies in the tropical Indian Ocean air–sea system during the positive IOD event
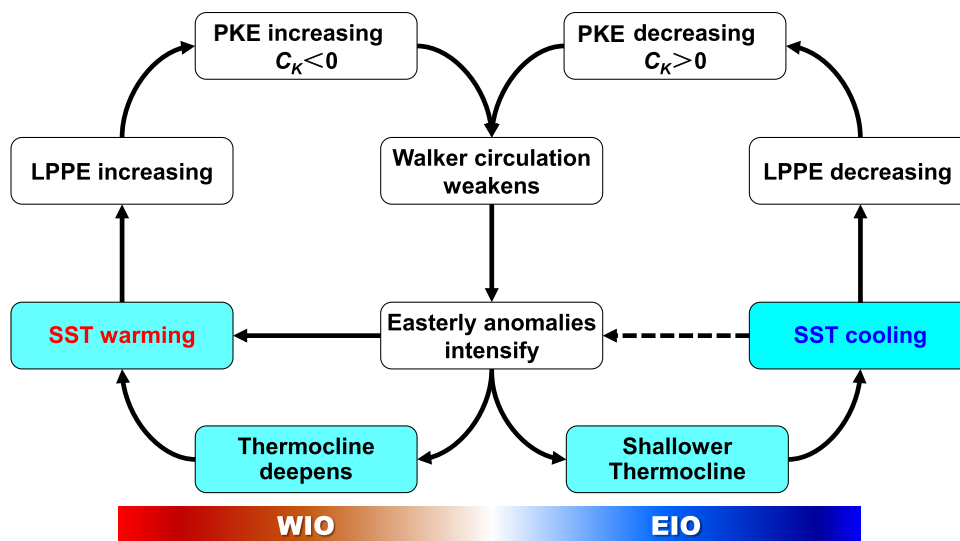
and thus the climatological Walker circulation. Meanwhile, the surface easterly anomalies strengthen and prevail along the west coast of Sumatra and raise the coastal thermocline to be shallow. After 1–2 months, stronger easterly anomalies force deepening of the thermocline in the IOD-W, leading to warmer SSTAs (Bjerknes 1969; Jin et al. 2006; Yokoi et al. 2008). Following the development of warmer SSTAs in the IOD-W, the PPE anomalies and C_K over the IOD-W have opposite characteristics to those in the east, and the climatological Walker circulation weakens further. As a result, the zonal winds in the lower troposphere remain strong, maintaining the SSTAs, which provide a positive air–sea feedback in the development and maintenance processes of IOD evolution.

7 Summary and discussion

This paper analyzes the relationships between the atmospheric PPE anomalies and the SSTAs over the Indian Ocean basin and the evolution of the PPE anomalies during an IOD event. Furthermore, the influence of atmospheric PPE anomalies on the atmospheric circulation and the effects of energy conversion on the evolution of the IOD in atmospheric processes are analyzed.

The PPE anomalies are significantly correlated with the IOD, corresponding to the anomalous variation in SST, and PKE anomalies are accordingly suppressed or enhanced over the equatorial Indian Ocean during the IOD event. The relation between DMI, PDI, and PKEI suggests that PPE is the key link between the underlying external forcing and PKE.

During the IOD event, PPE anomalies in the lower troposphere (1000–850 hPa) present a dipole pattern in response to the SSTAs and their evolution is essentially synchronous with that of the SSTAs. Negative PPE anomalies and

SSTAs first occur in the IOD-E. As the SSTAs intensify in the Indian Ocean, PPE anomalies develop into a noticeable dipole pattern over the tropical Indian Ocean from July to August. Then, negative PPE anomalies weaken over the IOD-E and positive PPE anomalies expand eastwards, covering the entire Indian Ocean. The change of PPE in the middle–upper troposphere lags that in the lower troposphere. PPE anomalies of the whole troposphere (1000–150 hPa) have the strongest response in the lower troposphere and have similar features to the PPE anomalies in the lower troposphere (1000–850 hPa).

During the IOD event, the IOD-W SSTAs have a delayed effect on the IOD-E SSTAs. The correlations between U-wind and SSTAs at the two poles suggest that the U-wind may cause this delayed effect through air–sea interaction, and the PPE has important impacts on the U-wind during the IOD event through energy conversion. When C_K is positive in the IOD-E, there is less conversion of PPE anomalies into PKE, and atmospheric PKE decreases, weakening the lower-level convergence of the climatological Walker circulation over the IOD-E. Anomalous surface easterly wind develops along the west coast of Sumatra and shallows the coastal thermocline, while warmer SSTAs in the IOD-W begin to develop. The PPE anomalies and C_K over the IOD-W are opposite to those in the east, and the anomalous easterly wind continues developing and the positive SSTAs in the IOD-W reach their maximum.

In this study we focused on the positive feedback mechanism of the IOD event. Further studies are needed to investigate the role of PPE in the transition from maturity to decay of the IOD event. In addition, the Indian Ocean lies upstream of the Asian summer monsoon region. As one of the principal sources of water vapor for the Asian summer monsoon, the impacts of Indian Ocean surface forcing on

energy conversion in the Asian monsoon region will be the focus of future work.

References

Annamalai H, Murtugudde R, Potemra J, Xie SP, Liu P, Wang B (2003) Coupled dynamics over the Indian Ocean: spring initiation of the zonal mode. Deep Sea Res Part II 50:2305–2330

Ashok K, Guan ZY, Yamagata T (2001) Impact of the Indian Ocean dipole on the relationship between the Indian monsoon rainfall and ENSO. Geophys Res Lett 28:4459–4502

Ashok K, Guan Z, Yamagata T (2003) A look at the relationship between the ENSO and the Indian Ocean dipole. J Meteorol Soc Jpn 80:41–56

Ashok K, Saji NH, Yamagata T (2004) Individual and combined influences of ENSO and Indian Ocean dipole on the Indian summer monsoon. J Clim 17:3141–3155

Behera SK, Yamagata T (2003) Influence of the Indian Ocean dipole on the Southern Oscillation. J Meteorol Soc Jpn 81:169–177

Bjerknes J (1966) A possible response of the atmospheric Hadley circulation to equatorial anomalies of ocean temperature. Tellus 18:820–829

Bjerknes J (1969) Atmospheric teleconnections from the equatorial Pacific. Mon Weather Rev 97:163–172

Ding RQ, Ha KJ, Li JP (2010) Interdecadal shift in the relationship between the East Asian summer monsoon and the tropical. Indian Ocean Clim Dyn 34:1059–1071

Dommenget D, Latif M (2002) A cautionary note on the interpretation of EOFs. J Clim 15:216–225

Dong D, He JH, Li JP (2016) Linkage between Indian Ocean dipole and two types of EI Niño and its possible mechanisms. J Trop Meteorol 22:172–180

Dong D, Li JP, Huyan L, Xue J (2017) Atmospheric energetics over the tropical Pacific during the ENSO Cycle. J Clim 30:3635–3654

Drbohlav HK, Gualdi S, Navarra A (2007) A diagnostic study of the Indian Ocean dipole mode in El Niño and Non-El Niño years. J Clim 20:2961–2977

Edmon HJ Jr (1978) A reexamination of limited-area available potential energy budget equations. J Atmos Sci 35:1655–1659

Feng M, Meyers G (2003) Interannual variability in the tropical Indian Ocean: a two-year time-scale of Indian Ocean Dipole. Deep Sea Res II 50:2263–2284

Gao L, Li JP (2007) Progress in the study of atmospheric energy efficiency (in Chinese). Adv Earth Sci 22:486–494

Gao L, Li JP (2012) Relationship and mechanism between perturbation potential energy and atmospheric general circulation anomalies. Chin J Geophys 55:359–374

Gao L, Li JP (2013) Impacts and mechanism of diabatic heating on atmospheric perturbation potential energy. Chin J Geophys 56:3255–3269

Gao L, Li JP, Ren HL (2006) Some characteristics of the atmosphere during an adiabatic process. Prog Nat Sci 16:644–648

Gu XZ (1990) A theoretical study of the available potential energy in a limited atmospheric region. Acta Meteorol Sin 48:248–252

Guan ZY, Yamagata T (2002) The unusual summer of 1994 in East Asia: IOD teleconnections. Geophys Res Lett 30:L01540. https://doi.org/10.1029/2002GL016831

Hong CC, Li T, Ho L, Kug JS (2008a) Asymmetry of the Indian Ocean dipole. Part I: observational analysis. J Clim 21:4834–4848

Hong CC, Lu MM, Kanamitsu M (2008b) Temporal and spatial characteristics of positive and negative Indian Ocean dipole with and without ENSO. J Geophys Res 113:D08107. https://doi.org/10.1029/2007JD009151

Hu Q, Tawaye Y, Feng S (2004) Variations of the Northern Hemisphere atmospheric energetics: 1948–2000. J Clim 17:1975–1986

Huyan LD, Li JP, Zhao S, Sun C, Dong D, Liu T, Zhao YF (2017) The impact of layer perturbation potential energy on the East-Asian summer monsoon. J Clim 30:7087–7103

Izumo T, Vialard J, Lengaigne M, de Boyer Montegut C, Behera SK, Luo J-J, Cravatte S, Masson S, Yamagata T (2010) Influence of the Indian Ocean Dipole on following year's El Niño. Nat Geosci 3:168–172

Jin FF, Kim ST, Bejarano L (2006) A coupled–stability index for ENSO. Geophys Res Lett 33:L23708. https://doi.org/10.1029/2006GL027221

Johnson DR (1970) The available potential energy of storms. J Atmos Sci 27:727–741

Kalnay E et al (1996) The NCEP/NCAR 40-year reanalysis project. Bull Am Meteorol Soc 77:437–471

Krishnamurthy V, Kirtman BP (2003) Variability of the Indian Ocean: relation to monsoon and ENSO. Q J R Meteorol Soc 129:1623–1646

Kumar KK, Rajagopalan B, Cane MA (1999) On the weakening relationship between the Indian monsoon and ENSO. Science 284:2156–2159

Li JP, Chou J (1997) Existence of atmosphere attractor. Sci China (Series E) 40:215–224

Li JP, Gao L (2006) Theory on perturbation potential energy and its applications—concept, expression and spatiotemporal structures of perturbation potential energy (in Chinese). Chin J Atmos Sci 30:834–848

Li CY, Mu MQ (2001) The influence of the Indian Ocean dipole on atmospheric circulation and climate. Adv Atmos Sci 18:831–842

Li JP, Wu GX, DX Hu (2011a) Ocean–atmosphere interaction over the joining area of Asia and Indian-Pacific ocean and its impact on the short-term climate variation in China (Volume I). China Meteorological, Beijing, pp 1–516

Li T, Zhang Y, Lu E, Wang D (2002) Relative role of dynamic and thermodynamic processes in the development of the Indian Ocean dipole: an OGCM diagnosis. Geophys Res Lett 29:21–25

Li T, Wang B, Chang CP, Zhang Y (2003) A theory for the Indian Ocean dipole-zonal mode. J Atmos Sci 60:2119–2135

Li JP, Wu GX, Hu DX (2011b) Ocean–atmosphere interaction over the joining area of Asia and Indian-Pacific ocean and its impact on the short-term climate variation in China (Volume II). China Meteorological, Beijing, pp 517–1081

Li JP, Wang QY, Li YJ, Zhang JW (2016a) Climatological research on tropical cyclones in terms of energetics: review and perspective. J Beijing Norm Univ (Natural Science) 52:705–713

Li JP, Zhao S, Li YJ, Wang L, Sun C (2016b) On the role of perturbation potential energy in variability of the East Asian summer monsoon: current status and prospects. Adv Earth Sci 31:115–125

Lorenz EN (1955) Available potential energy and the maintenance of the general circulation. Tellus 7:157–167

Luo JJ, Zhang RC, Behera SK, Masumoto Y (2010) Interaction between El Niño and extreme Indian Ocean dipole. J Clim 23:726–742

Murtugudde R, McCreary JP, Busalacchi AJ (2000) Oceanic processes associated with anomalous events in the Indian Ocean with relevance to 1997–1998. J Geophys Res 105:3295–3306

Nicholls N, Drosdowsky W (2001) Is there an equatorial Indian Ocean SST dipole, independent of the El Niño–Southern Oscillation? In: American meteorological society 81st annual meeting, Albuquerque, NM, 14–19 January 2001

Oort AH (1964) On estimates of the atmospheric energy cycle. Mon Weather Rev 92:483–493

Oort AH (1971) The observed annual cycle in the meridional transport of atmospheric energy. J Atmos Sci 28:325–339

Oort AH, Ascher SC, Levitus S, Peixóto JP (1989) New estimates of the available potential energy in the world ocean. J Geophys Res 94:3187–3200

Peixóto JP, Oort AH (1974) The annual distribution of atmospheric energy on a planetary scale. J Geophys Res 79:2149–2159

Rao SA, Luo JJ, Behera SK, Yamagata T (2009) Generation and termination of Indian Ocean dipole events in 2003, 2006 and 2007. Clim Dyn 33:751–767

Rayner NA, Parker DE, Horton EB, Folland CK, Alexander LV, Rowell DP (2003) Global analyses of sea surface temperature, sea ice, and night marine air temperature since the late nineteenth century. J Geophys Res 108:4407

Saji NH, Goswami BN (1999) A dipole mode in the tropical Indian Ocean. Nature 401:360–363

Saji NH, Yamagata T (2003) Possible impacts of Indian Ocean dipole mode events on global climate. Clim Res 25:151–169

Smith PJ (1969a) On the contribution of a limited region to the global energy budget. Tellus 21:202–207

Smith PJ, Horn LH (1969b) A computational study of the energetics of a limited region of the atmosphere. Tellus 21:193–201

Wang L, Li JP, Guo Y (2012) Governing equations of atmospheric layer perturbation potential energy and its applications—energy budget of the South China Sea summer monsoon activity. Chin J Atmos Sci 36:769–783

Wang L, Wang Z, Li Y, Zheng F (2015) The oscillation of the perturbation potential energy between the extra-tropics and tropics in boreal winter. Atmos Sci Lett 16:119–126

Wang H, Murtugudde R, Kumar A (2016) Evolution of Indian Ocean dipole and its forcing mechanisms in the absence of ENSO. Clim Dyn 47:2481–2500

Wang QY, Li JP, Li YJ, Xue JQ, Zhao S, Xu YD, Wang YH, Zhang YZ, Dong D, Zhang JW (2018) Modulation of tropical cyclone tracks over the western North Pacific by intra-seasonal Indo-western Pacific convection oscillation during the boreal extended summer. Clim Dyn. https://doi.org/10.1007/s00382-018-4264-6

Webster PJ, Moore AM, Loschnigg JP, Leben RR (1999) Coupled ocean–atmosphere dynamics in the Indian Ocean during 1997–98. Nature 401:356–360

Yamagata T, Behera SK, Luo JJ, Masson S, Jury MR, Rao SA (2004) Coupled ocean–atmosphere variability in the tropical Indian Ocean. Am Geophys Union 147:189–212

Yang Y, Xie SP, Wu L, Kosaka Y, Lau NC, Vecchi GA (2015) Seasonality and predictability of the Indian Ocean dipole mode: ENSO forcing and internal variability. J Clim 28:8021–8036

Yokoi T, Tozuka T, Yamagata T (2008) Seasonal variation of the Seychelles Dome. J Clim 21:3740–3754

Zhang YZ, Li JP, Xue JQ, Feng J, Wang QY, Xu YD, Wang YH (2018) Impact of the South China Sea summer monsoon on the Indian Ocean dipole. J Clim 31:6557–6572

Zhou L, Murtugudde R, Chen D, Tang Y (2017) Seasonal and interannual variabilities of the central Indian Ocean. J Clim 30:6505–6520